Supplemental Information

Efficient 1.77 eV-Bandgap Perovskite and All-Perovskite Tandem Solar Cells Enabled by Long-Alkyl Phosphonic Acid

Hongling Guan[†,a,b,d] Shiqiang Fu[†,a] Guojun Zeng,[a] Weiqing Chen,[a] Chen Wang,[a] Hongsen Cui,[a] Dexin Pu,[a] Peng Jia,[a] Weiwei Meng,*[c] Guojia Fang,*[a] Weijun Ke*[a,d]

[a]Key Lab of Artificial Micro- and Nano-Structures of Ministry of Education, School of Physics and Technology, Wuhan University, Wuhan 430072, P. R. China

[b]Department of Electrical and Electronic Engineering, Chongqing University of Technology, Chongqing 400054, P. R. China

[c]South China Academy of Advanced Optoelectronics, South China Normal University, Guangzhou 510006, P. R. China

[d]Wuhan University Shenzhen Research Institute, Shenzhen 518055, P. R. China

*Corresponding Email: wwmeng@m.scnu.edu.cn; gjfang@whu.edu.cn; weijun.ke@whu.edu.cn

† These authors contributed equally to this work.

Experimental Section

Materials

Dodecylphosphonic Acid (DDPA) was purchased from Aladdin Co. Ltd. [4-(3,6-Dimethyl-9H-carbazol-9-yl)butyl]phosphonic Acid (Me-4PACz) were purchased from Tokyo Chemical Industry Co. Ltd. Fullerene (C_{60}) and bathocuproine (BCP) and 1,3-propyldiammonium diiodide ($PDAI_2$) were purchased from Xi'an Polymer Light Technology Corp. Formamidinium iodide (FAI), lead iodide (PbI_2), Cesium iodide (CsI), lead bromide ($PbBr_2$) and NiO_x nanoparticles were bought from Advanced Election Technology Co. Ltd. Isopropanol (IPA), lead thiocyanate ($Pb(SCN)_2$)potassium iodide (KI), N, N-dimethylformamide (DMF), and dimethylsulfoxide (DMSO) were bought from Sigma-Aldrich. Diethyl ether was purchased from Sinopharm Group. Tetrakis(dimethylamino) tin (IV) (99.9999%) for atomic layer deposited (ALD) SnO_2 was purchased from Nanjing Ai Mou Yuan Scientific Equipment Co., Ltd.

Film and device fabrication

WBG perovskites

1.2 mol L^{-1} of WBG (1.77 eV-bandgap) perovskite precursor solutions with a composition of $FA_{0.8}Cs_{0.2}Pb(I_{0.6}Br_{0.4})_3$ were prepared by dissolving CsI, FAI, $PbBr_2$, and PbI_2 in a mixed solvent of DMF and DMSO with a volume ratio of 4:1. The precursor solutions were then added with 1 mol% of KI and 1 mol% $Pb(SCN)_2$ and x mol% DDPA (x = 0.1, 0.2 and 0.5). Then, the perovskite precursors were stirred at 65 ºC for 12 h and filtered using a 0.22 μm PTFE membrane before use.

Fabrication of WBG PSCs

Ultra-sonication cleaned glass/ITO substrates with deionized water, acetone, and ethanol for 30 min, respectively. Before use, the substrates were treated with ultraviolet ozone for 15 min and then transferred into an N_2-filled glovebox. Subsequently, the solutions of NiO_x nanoparticles were spin-coated on the glass/ITO substrates at 3,000 r.p.m. for 30 s, followed by annealing at 130 °C for 20 min (about 10 mg/mL in deionized water) and then transferred into an N_2-filled glovebox. Subsequently, Me-4PACz (0.3 mg mL^{-1}) in ethanol was spin-coated on the NiO_x film at 4,000 rpm for 30 s and then annealed at 100 °C for 10 min.

40 μL of as-prepared perovskite precursor solutions were dropped on the substrates and then spin-coated with the first step at 1000 r.p.m. for 10 s and the second step at 5000 r.p.m for 60 s. Subsequently, 350 μL of diethyl ether was dripped on the substrates at the 45^{th} second of the second step, followed by annealing at 60 ℃ for 2 min and 100 ℃ for 20 min. Typically, $PDAI_2$ molecules were dissolved in IPA with a concentration of 2 mg/mL. Then, $PDAI_2$ solutions (80 μL) were spin-coated onto the as-prepared perovskite films at 4,000 r.p.m. for 30 s, followed by annealing at 100 °C for 5 min. To complete solar cell fabrication, all the substrates were transferred into a thermal evaporation chamber, and 22 nm of C_{60}, 8 nm of BCP or 20 nm of SnO_2, and 100 nm of copper (Cu) were evaporated successively at 2×10^{-4} Pa.

Fabrication of semi-transparent WBG PSCs

The semi-transparent PSCs were prepared referring to our previous work.[1] The precursors of deionized water and tetrakis(dimethylamino) tin (IV) were used to

fabricate SnO_2. 100 nm of ITO was sputtered at a power of 100 W under an Ar pressure of 0.2 Pa. To complete the solar cell fabrication, all the substrates were transferred into a thermal evaporation chamber, and 100 nm of silver (Ag) was evaporated successively at 2 $\times 10^{-4}$ Pa.

Fabrication of NBG PSCs[2]

The filtered poly(3,4-ethylenedioxythiophene)/poly(styrenesulfonate) (PEDOT:PSS) solutions were spin-coated on the glass/ITO substrates at 6000 rpm for 30 s and then the glass/ITO substrates were annealed at 140 °C for 15 min. In the following, 50 μL of the filtered $FA_{0.7}MA_{0.3}Pb_{0.5}Sn_{0.5}I_3$ precursors were deposited on the substrates using a two-step spin-coating process in an N_2-filled glovebox, with the first step at 1000 r.p.m. for 10 s and the second step at 6000 r.p.m. for 50 s. During the second spin-coating step, 500 μL of chlorobenzene (CB) was dropped onto the spinning substrates at the twentieth second of the second step, followed by annealing at 100 ℃ for 9 min. Finally, to complete the solar cell fabrication, C_{60} (20 nm)/BCP (7 nm)/Cu (100 nm) were sequentially evaporated onto the substrates by thermal evaporation.

Fabrication of all-perovskite TSCs

The fabrication of WBG PSCs was completed as described above up to the deposition of 20 nm of SnO_2. Subsequently, 1 nm of Au was deposited by thermal evaporation. Next, PEDOT:PSS (diluted at a 1:1 volume ratio in ethanol) was spin-coated onto the WBG subcell at 6,000 rpm for 30 s and annealed at 100 °C for 10 min. Substrates were then cooled and transferred to an N_2–filled glovebox for the deposition of the NBG subcell.

Characterization and analysis

Film characterization

DeltaFlex fluorescence spectrometer (HORIBA) with a center wavelength of 481 nm semiconductor laser and a time-correlated single-photon counting (TCSPC) module were used to obtain photoluminescence (PL) and time-resolved photoluminescence (TRPL) of films. Kelvin probe force microscopy (KPFM) images of perovskites were implemented by using a Bruker dimension icon under a peak force mode. X-ray photo-electron spectroscopy (XPS) and UV photoelectron spectroscopy (UPS) spectra were carried out using an XPS/UPS system (Thermo Scientific, Escalab 250Xi). X-ray diffraction (XRD) analysis was performed using a Bruker AXS, D8 Advance instrument to characterize the crystal structures and phases of perovskite films. Scanning electron microscopy (SEM) (Zeiss SIGMA) with an accelerating voltage of 5 keV was performed to observe the morphology of the films. Absorption spectra of films were implemented by using a spectrophotometer (UV-vis, mini UV-1208 model, Shimadzu). Fourier transform infrared (FTIR) spectra of the samples were measured using a NICOLET iS50 FT-IR Spectrometer (Thermo Scientific, ATR: SMART iTR Diamond).

Device characterization

Current-voltage (*J-V*) curves and steady-state power outputs of PSCs were measured by masking the active area with a metal mask (the hole area was 0.070225 cm^2) under air mass 1.5 global (AM 1.5 G) conditions (Enli Technology Co. Ltd) in a nitrogen atmosphere. *J-V* measurements were performed with a scan rate of 20 mV/s ranging

from 1.34 to -0.1 V and then reversed again from -0.1 to 1.34 V with a dwell time of 25 ms. A QE/Incident photon-to-electron conversion efficiency (IPCE) system (Enli Technology Co. Ltd) was used to obtain external quantum efficiency (EQE) results.

Admittance characterization

Capacitance-voltage (*C*-*V*) curves were carried out using a CHI760E electrochemical workstation (Shanghai Chenhua Instruments). The measurements were conducted at a frequency of 1 kHz and DC bias voltages ranging from 1.4 to 0 V, with a scan rate of 20 mV/s, to test the corresponding capacitance at various bias voltages. Admittance spectroscopy (AS) measurements were performed on a CHI760E electrochemical workstation at different temperatures ranging from 320 to 250 K in the dark. A small AC disturbed voltage of 20 mV, a DC bias voltage of 0 V, a relatively low vacuum (< 10 Pa), and a frequency range from 1 Hz to 100 kHz were maintained during the AS measurements.

According to a depletion approximation equation (Mott–Schottky) (formula 1 and 2), the built-in potential (V_{bi}) and depletion width (W) of the devices were determined from the C^{-2}-V curves:[3]

$$\frac{A^2}{C^2} = \frac{2(V_{bi} - V)}{q\varepsilon\varepsilon_0 N} \tag{1}$$

$$W = \sqrt{\frac{2\varepsilon\varepsilon_0 V_{bi}}{qN}} \tag{2}$$

Where A, C, V, ε, ε_0, q, and N are the active area, capacitance, applied bias voltage, relative dielectric constant, permittivity of vacuum, elementary charge, and doping

profile, respectively.

Furthermore, low-pressure AS (< 10 Pa) measurements were implemented to analyze both the distribution and density of trap states in the perovskite films. The characteristic transition angular frequency ($\omega = \omega_0$) was determined through AC signal transformation at each temperature, the Arrhenius plots of the transition frequencies were fitted according to the following formula (3),[3-4]

$$\omega_0 = \beta T^2 exp(-\frac{E_a}{k_b T}) \tag{3}$$

Where β and E_a are the temperature-independent parameter and trap activation energy, respectively. Then, the energy level distribution of defects and trap states density (N_T) at room temperature were estimated using the following formulae (4) and (5):[3-4]

$$E_\omega = k_b T ln(\frac{\beta T^2}{\omega}) \tag{4}$$

$$N_T(E_\omega) = -\frac{V_{bi}\, dC\ \ \omega}{qWd\omega k_b T} \tag{5}$$

where E_ω represents the energy level difference between the defect and the conduction band maximum.

2T TSC measurements

Current-voltage (*J-V*) curves and steady-state power outputs of PSCs were measured by masking the active area with a metal mask (the hole area was 0.070225 cm^2) under air mass 1.5 global (AM 1.5 G) conditions (Enli Technology Co. Ltd) in a nitrogen

atmosphere. *J-V* measurements were fulfilled with a scan rate of 20 mV/s ranging from 2.20 to -0.1 V and then reversed again from -0.1 to 2.20 V with a dwell time of 25 ms.

4T TSC measurements

For 4T TSC measurements, the PCE of the top semi-transparent WBG PSCs was first measured. Silicone oil was applied in the air gap between the semi-transparent cells and the NBG cells to minimize optical loss, as reported previously.[5] Subsequently, the PCE of the bottom NBG PSCs was tested after passing through light filtered by the top semi-transparent WBG PSCs. The PCE of 4T all-perovskite TSCs was equal to the sum of the efficiencies of the semi-transparent WBG and filtered NBG PSCs.

DFT calculations

Ordered $FAPb(I_{0.5}Br_{0.5})_3$ ($Z = 2$) configuration with the lowest total energy was chosen as matrix to approximately mimic experimental WBG perovskite composition with I:Br = 0.6:0.4. Perovskite surfaces with FAI and $Pb(I/Br)_2$ terminations were considered, representing the preferred axial occupation of iodine and equatorial ordering of Br in mixed halide perovskites [6]. Both the perfect and defective surfaces with seven atomic layers were relaxed using the CP2K package[7] at the Perdew–Burke–Ernzerhof (PBE) level[8]. The bottom three layers were fixed to mimic the bulk constraint. A vacuum thickness of 15 Å was used to avoid the image interaction. The in-plane lattice constants were 17.97 Å and 24.14 Å, respectively. The double-ξ valence polarization basis set [9] in combination with the norm-conserving Goedecker–Teter–Hutter pseudopotential[10-11] is employed by considering only the gamma point, and an energy cut-off of 800 Rydberg is set. Grimme's D3 correction was considered to dispose of the van der

Waals interactions[12-13]. The density of states (DOS) was calculated using the Vienna ab initio simulation package code[14-15] with projector-augmented wave potentials58. The generalized gradient approximation (GGA) of PBE functional was used for exchange correlation. The cutoff energy for basis functions was 520 eV and the Γ-only *k* sampling was chosen. The surface defect formation energy was calculated as the total energy difference between the perfect surface and defective surface as well as pure elements.

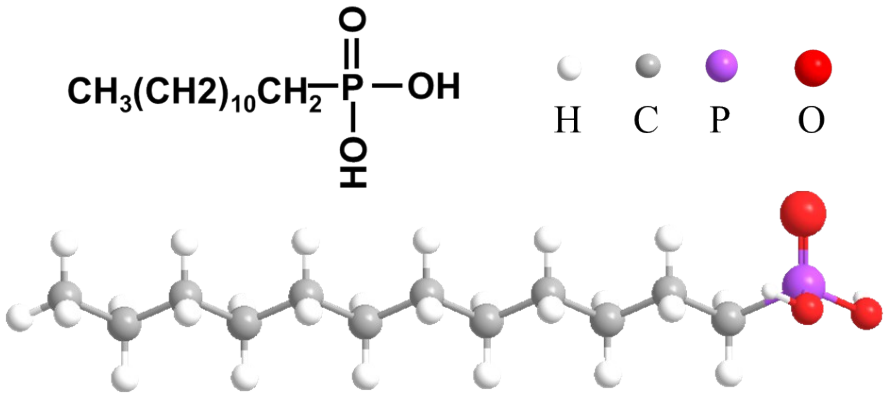

Figure S1. (a) The chemical structure of DDPA.

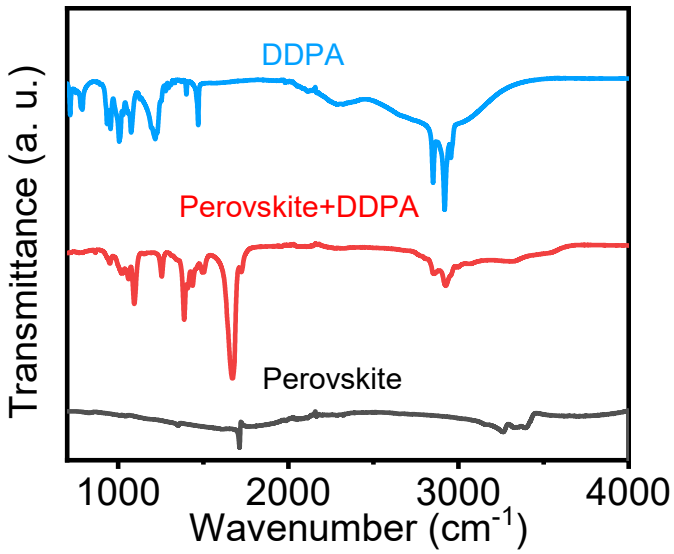

Figure S2. FTIR spectra of pure DDPA and perovskite powders without and with DDPA addition.

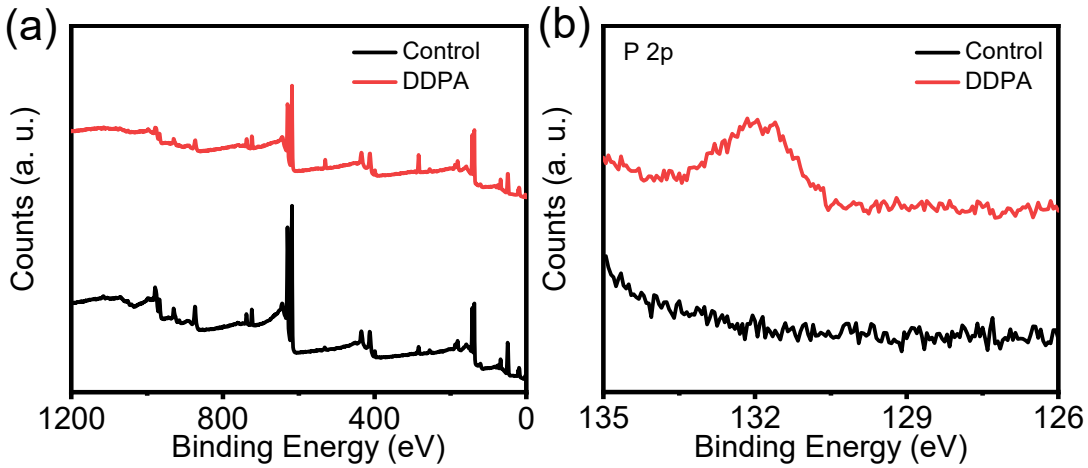

Figure S3. (a) Total scan range plots, and (b) P 2p of XPS surveys of perovskite films without and with DDPA addition.

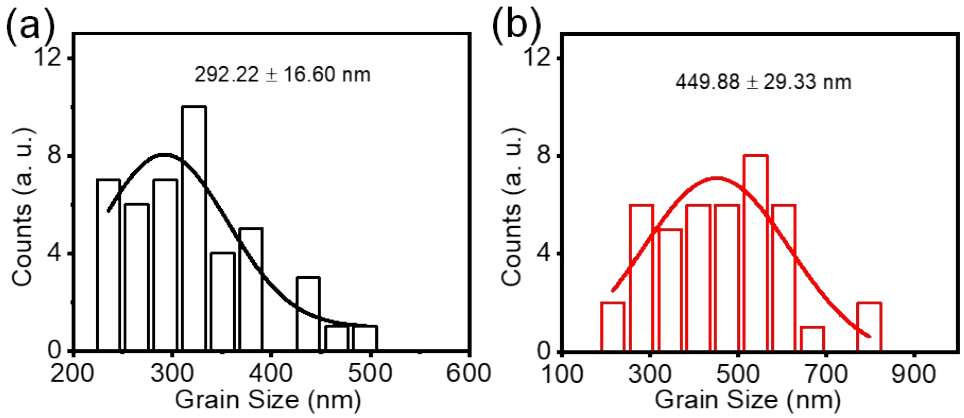

Figure S4. Grain size statistics of perovskite films (a) without and (b) with DDPA treatment. The average grain sizes of the control and DDPA-treated samples were 292.22 ± 16.60 nm and 449.88 ± 29.33 nm, respectively.

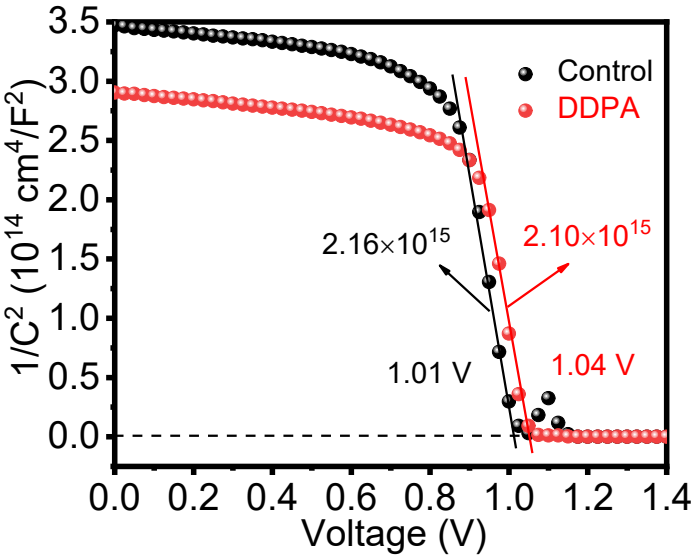

Figure S5. Mott–Schottky analysis of representative control and DDPA-treated PSCs at 1000 Hz in the dark. The V_{bi} values were 1.01 and 1.04 V for the WBG PSCs without and with DDPA treatment, and the corresponding depletion width (W) values were 100.90 and 100.96 nm, respectively.

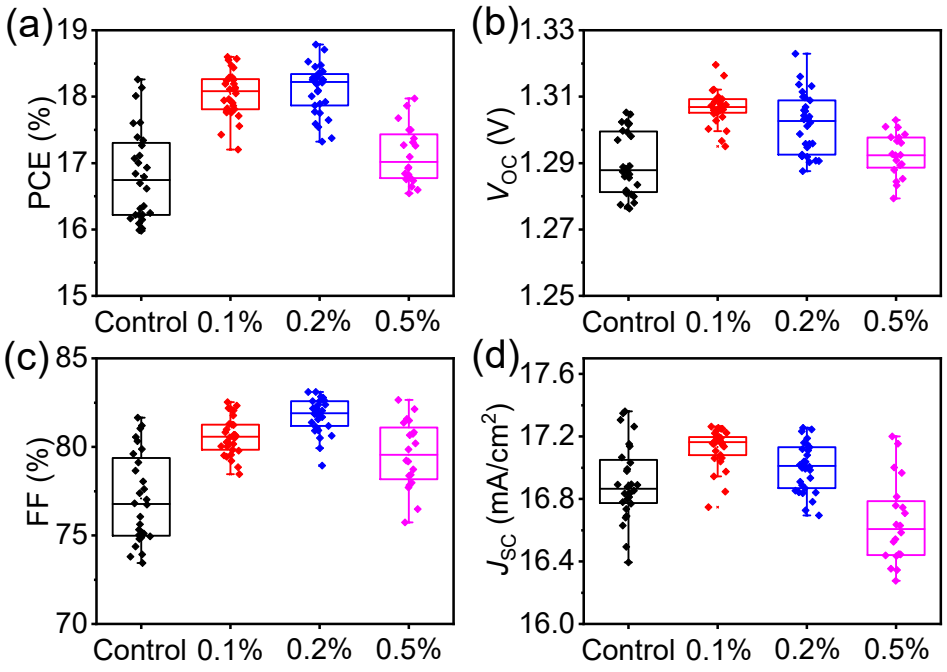

Figure S6. (a) PCE, (b) V_{OC}, (c) FF, and (d) J_{SC} statistics of PSCs using 2PACz HTLs with various concentrations of DDPA treatment. The optimum concentration of DDPA was around 0.2%. Each data was extracted from 14 cells.

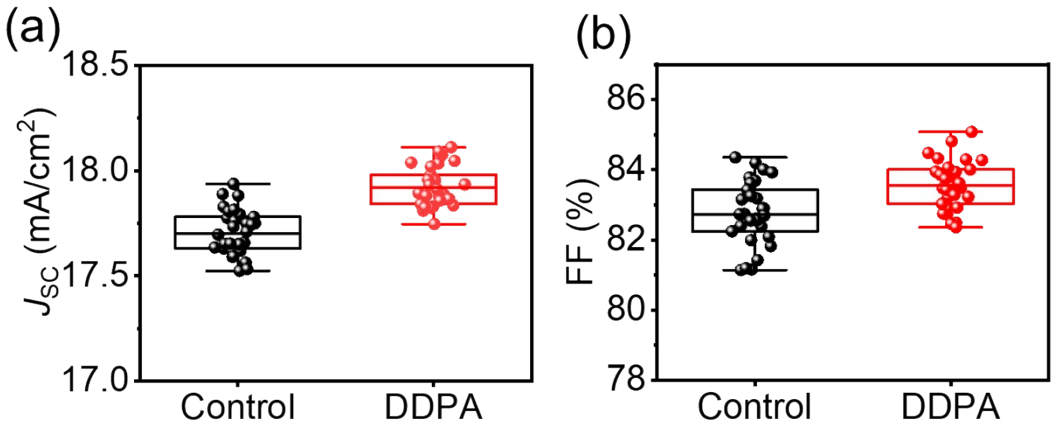

Figure S7. (a) J_{sc} and (b) FF statistics for two types of devices. Each parameter was extracted from 30 cells. The device structure was glass/ITO/NiO_x+Me-4PACz/WBG perovskites/C_{60}/BCP/Cu).

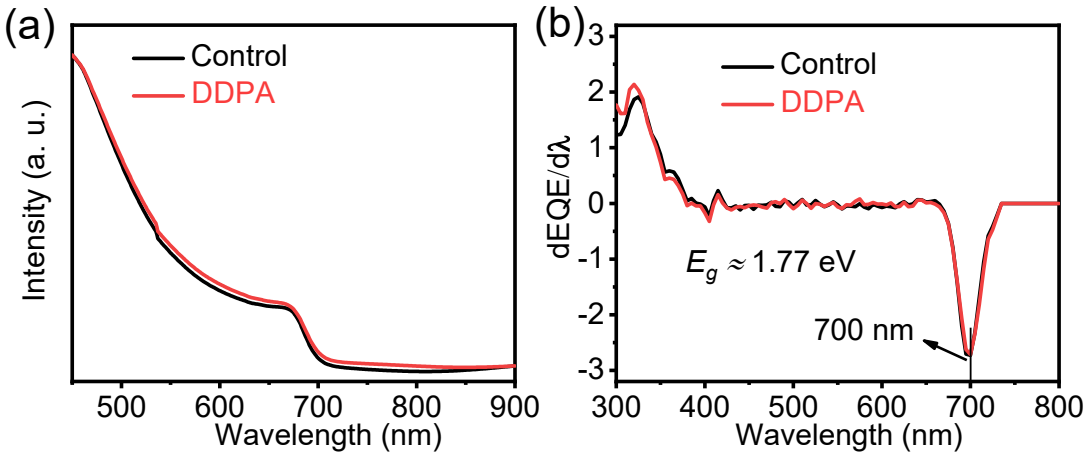

Figure S8. (a) Absorption spectra of control and DDPA-treated WBG perovskite films. (b) The first derivatives of the corresponding EQE curves of control and DDPA-treated WBG PSCs.

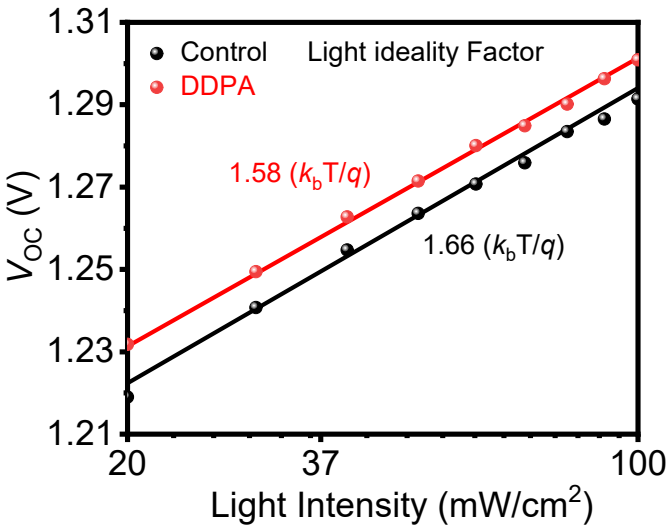

Figure S9. (a) Light-intensity-dependent V_{OC} of control and DDPA-treated PSCs.

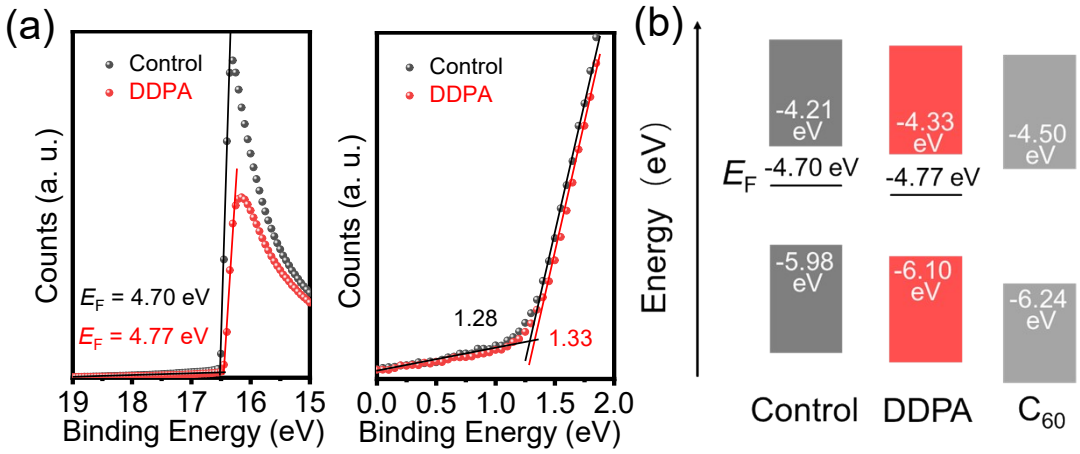

Figure S10. (a) UPS spectra of control and DDPA-treated perovskite films. (b) Schematic energy-level diagram of control, DDPA-treated perovskite films, and C_{60}.

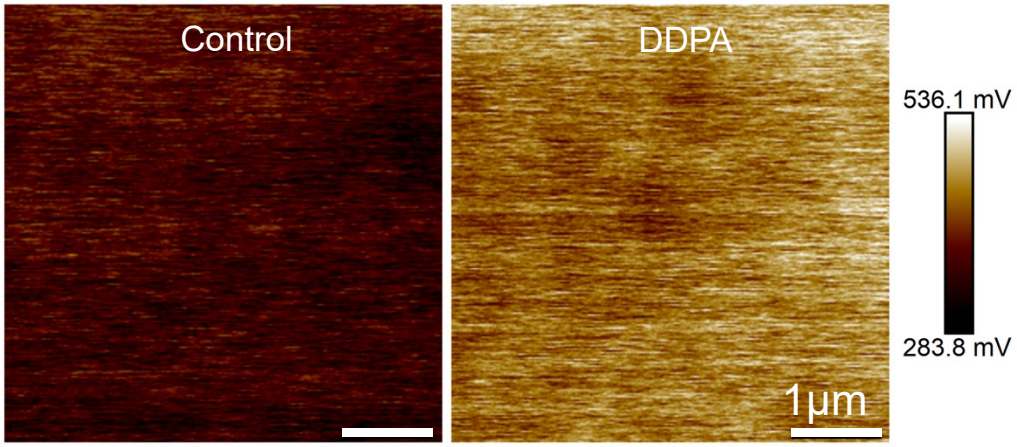

Figure S11. KPFM images of two types of perovskite films. The surface potential bars represent the contact potential differences between the probe and the measured samples (i.e., $P_{measured} = P_{sample} - P_{probe}$).

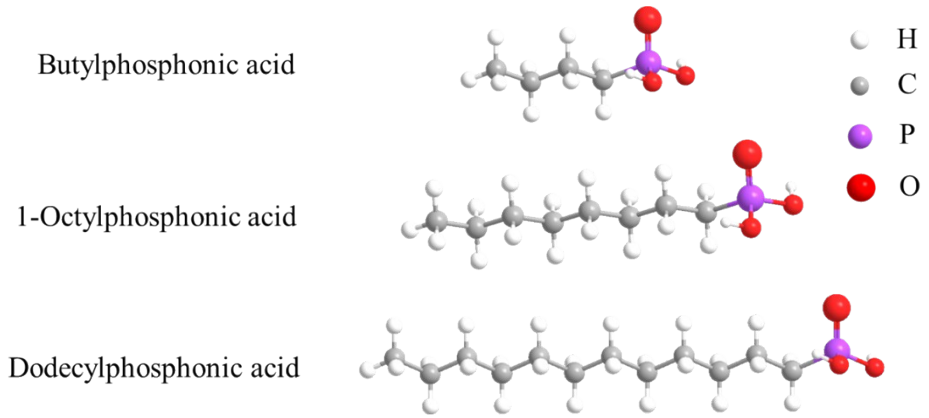

Figure S12. The molecular structures of three types of long-alkyl phosphonic acids: butylphosphonic acid, 1-Octylphosphonic acid, and DDPA.

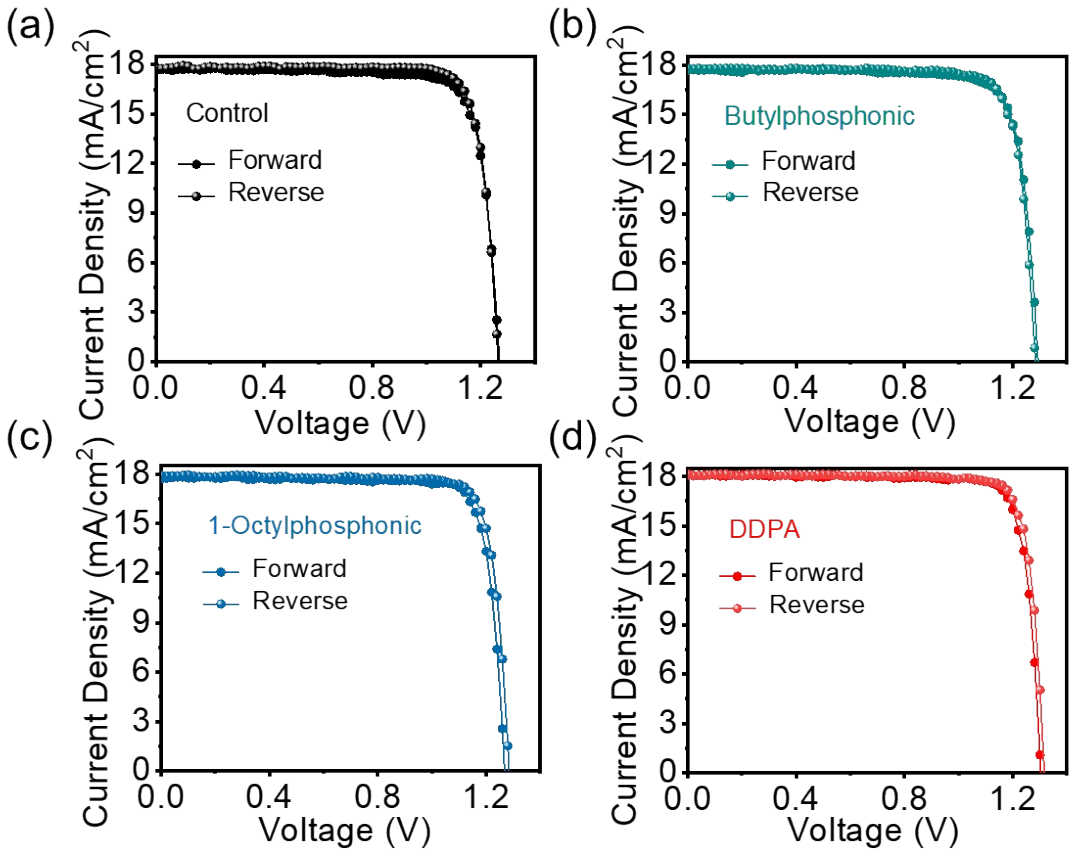

Figure S13. *J–V* curves for the (a) control, (b) butylphosphonic acid, (c) 1-octylphosphonic acid, and (d) DDPA-treated PSCs (The device structure was glass/ITO/NiO_x+Me-4PACz/WBG perovskites/C_{60}/BCP/Cu).

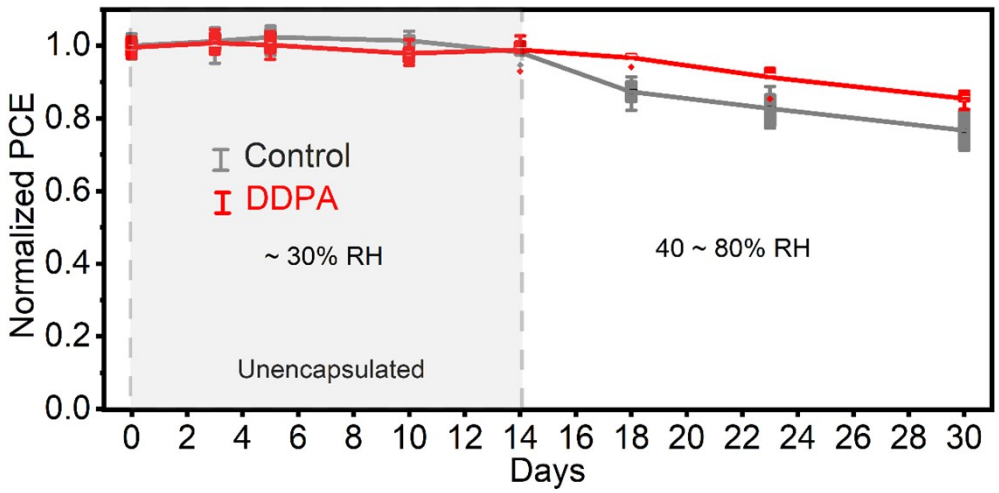

Figure S14. Long-term storage stability of unencapsulated devices under an atmospheric environment at 20 ± 5 °C and 30–80% RH (PCE data extracted from three cells for each condition).

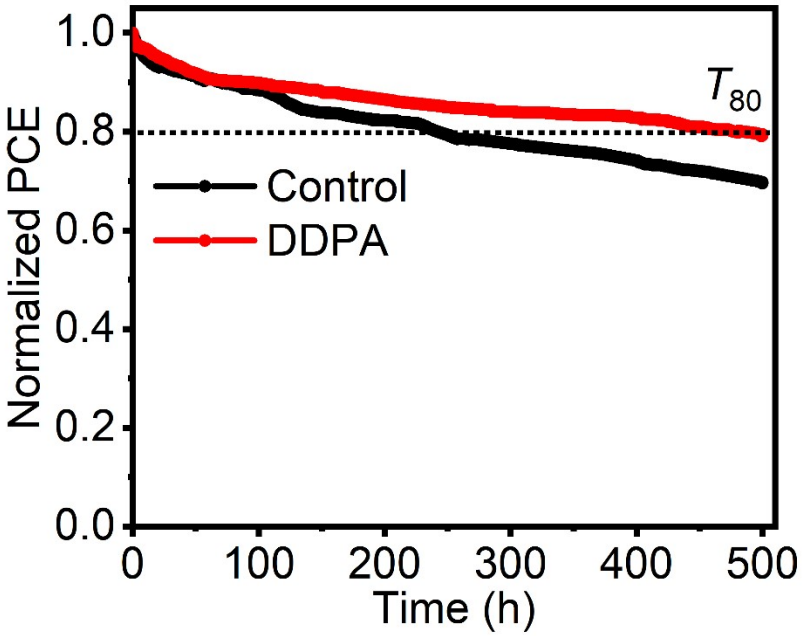

Figure S15. MPP tracking of single-junction control and DDPA-treated WBG PSCs under simulated 1-sun illumination in an N_2-filled glovebox at approximately 55°C without a cooling system. T_{80} represents the time required for the device efficiency to drop to 80% of its initial value.

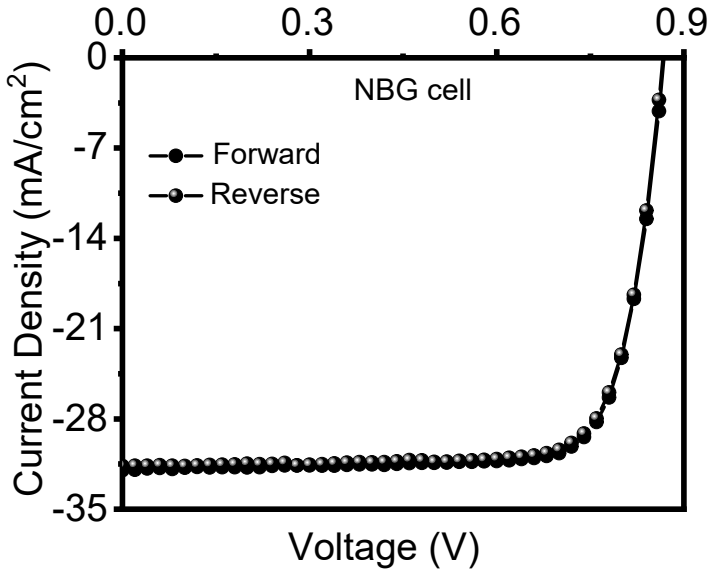

Figure S16. *J-V* curve of an original NBG PSC.

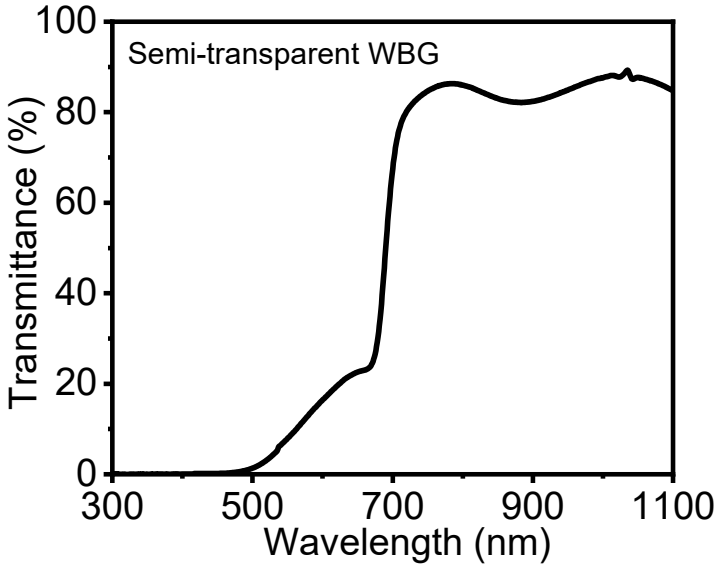

Figure S17. Transmittance spectrum of a semi-transparent WBG PSC.

Table S1. TRPL fitting results of WBG perovskite films coated on glass/ITO/HTL substrates.

Sample	τ_1 (ns)	τ_2 (ns)	τ_{avg} (ns)
Control	8.50	75.47	69.78
DDPA	24.07	159.73	143.07

Table S2. Photovoltaic parameters obtained from the control and DDPA-treated PSCs (The device structure was glass/ITO/NiO_x+Me-4PACz/WBG perovskites/C_{60}/BCP/Cu).

Sample	Scan direction	V_{OC} (V)	J_{SC} (mA·cm^{-2})	FF (%)	PCE (%)
Control	Forward	1.27	17.65	82.61	18.52
	Reverse	1.27	17.84	83.32	18.87
DDPA	Forward	1.31	17.98	84.59	19.97
	Reverse	1.32	18.09	84.40	20.20

Table S3. Photovoltaic parameters obtained from the control, butylphosphonic acid, 1-octylphosphonic acid, and DDPA-treated PSCs. The device structure was glass/ITO/NiO_x+Me-4PACz/WBG perovskites/C_{60}/BCP/Cu.

Sample	Scan direction	V_{OC} (V)	J_{SC} (mA·cm^{-2})	FF (%)	PCE (%)
Control	Forward	1.27	17.69	81.75	18.37
	Reverse	1.26	17.81	83.56	18.75
butylphosphonic	Forward	1.29	17.75	81.66	18.71
	Reverse	1.28	17.80	83.04	18.91
1-octylphosphonic	Forward	1.27	17.75	83.83	18.90
	Reverse	1.28	17.90	83.95	19.23
DDPA	Forward	1.30	18.07	84.57	19.86

Reverse	1.31	18.09	85.03	20.15

Table S4. Statistics of performance parameters of 2T perovskite/perovskite TSCs.

Sample	V_{OC} (V)	J_{SC} (mA·cm^{-2})	FF (%)	PCE (%)
2-Terminal tandem	2.12 ± 0.01	15.30 ± 0.15	80.77 ± 1.07	26.17 ± 0.60

Table S5. Photovoltaic parameters of a WBG PSC, an NBG PSC, and their 4T TSC.

Sample	Scan direction	V_{OC} (V)	J_{SC} (mA·cm^{-2})	FF (%)	PCE (%)	SPO (%)
Semi-transparent WBG PSC	Forward	1.30	16.88	83.36	18.26	18.41
	Reverse	1.30	16.80	84.55	18.49	
Original NBG PSC	Forward	0.87	31.99	78.11	21.66	NA
	Reverse	0.86	31.64	78.40	21.46	
Filtered NBG PSC	Forward	0.84	15.16	79.62	10.16	10.05
	Reverse	0.84	15.15	79.56	10.16	
4-Terminal tandem	Forward				28.42	28.46
	Reverse	-	-	-	28.65	

Table S6. Summary of the state-of-the-art 4T perovskite/perovskite TSCs.

year	PCE (%)	References
2017	21	[16]
2018	23	[5]
2019	25.4	[17]
2020	23.6	[18]
2021	24.8	[19]
2021	24.8	[20]
2022	26.01	[21]
2022	25.17	[22]
2023	26.30	[23]
2023	26.64	[24]
2023	26.48	[25]
2023	27.07	[26]
2023	27.46	[2]
2023	27.64	[27]
2023	28.05	[28]
2023	28.06	[1]
2024	28.35	[29]
2024	28.65	This work

References

[1] H. Guan, S. Zhou, S. Fu, D. Pu, X. Chen, Y. Ge, S. Wang, C. Wang, H. Cui, J. Liang, X. Hu, W. Meng, G. Fang, W. Ke, *Adv. Mater.* **2023**, 36, 2307987.

[2] W. Chen, H. Guan, L. Huang, J. Zhou, S. Zhou, D. Pu, G. Zeng, C. Wang, Y. Ge, C. Wang, W. Shen, H. Fang, G. Li, Q. Lin, G. Fang, W. Ke, Q. Liu, *Sol. RRL* **2023**, 230089.

[3] S. Ye, H. Rao, Z. Zhao, L. Zhang, H. Bao, W. Sun, Y. Li, F. Gu, J. Wang, Z. Liu, Z. Bian, C. Huang, *J. Am. Chem. Soc.* **2017**, 139, 7504.

[4] T. Walter, R. Herberholz, C. Müller, H. W. Schock, *J. Appl. Phys.* **1996**, 80, 4411.

[5] D. Zhao, C. Wang, Z. Song, Y. Yu, C. Chen, X. Zhao, K. Zhu, Y. Yan, *ACS Energy Lett.* **2018**, 3, 305.

[6] M. A. Hope, M. Cordova, A. Mishra, U. Gunes, A. Caiazzo, K. Datta, R. A. J. Janssen, L. Emsley, *Angew. Chem. Int. Ed.* **2024**, 63, e202314856.

[7] T. D. Kühne, M. Iannuzzi, M. Del Ben, V. V. Rybkin, P. Seewald, F. Stein, T. Laino, R. Z. Khaliullin, O. Schütt, F. Schiffmann, *J. Chem. Phys.* **2020**, 152, 194103.

[8] J. P. Perdew, K. Burke, M. Ernzerhof, *Phys. Rev. Lett.* **1996**, 77, 3865.

[9] J. VandeVondele, J. Hutter, *J. Chem. Phys.* **2007**, 127, 114105.

[10] M. Krack, *Theoretical Chemistry Accounts* **2005**, 114, 145.

[11] S. Goedecker, M. Teter, J. Hutter, *Phys. Rev. B* **1996**, 54, 1703.

[12] S. Grimme, *J. Comput. Chem.* **2006**, 27, 1787.

[13] S. Grimme, J. Antony, S. Ehrlich, H. Krieg, *J. Chem. Phys.* **2010**, 132, 154104.

[14] G. Kresse, J. Hafner, *Phys. Rev. B* **1993**, 47, 558.

[15] G. Kresse, J. Furthmüller, *Phys. Rev. B* **1996**, 54, 11169.

[16] D. Zhao, Y. Yu, C. Wang, W. Liao, N. Shrestha, C. R. Grice, A. J. Cimaroli, L. Guan, R. J. Ellingson, K. Zhu, X. Zhao, R.-G. Xiong, Y. Yan, *Nat. Energy* **2017**, 2, 17018.

[17] J. Tong, Z. Song, D. H. Kim, X. Chen, C. Chen, A. F. Palmstrom, P. F. Ndione, M. O. Reese, S. P. Dunfield, O. G. Reid, J. Liu, F. Zhang, S. P. Harvey, Z. Li, S. T. Christensen, G. Teeter, D. Zhao, M. M. Al-Jassim, M. F. A. M. van Hest, M. C. Beard,

S. E. Shaheen, J. J. Berry, Y. Yan, K. Zhu, *Science* **2019**, 364, 475.

[18] S. Moghadamzadeh, I. M. Hossain, T. Duong, S. Gharibzadeh, T. Abzieher, H. Pham, H. Hu, P. Fassl, U. Lemmer, B. A. Nejand, U. W. Paetzold, *J. Mater. Chem. A* **2020**, 8, 24608.

[19] S. Moghadamzadeh, I. M. Hossain, M. Loy, D. B. Ritzer, H. Hu, D. Hauschild, A. Mertens, J.-P. Becker, A. A. Haghighirad, E. Ahlswede, L. Weinhardt, U. Lemmer, B. A. Nejand, U. W. Paetzold, *ACS Appl. Mater. Inter.* **2021**, 13, 46488.

[20] H. Hu, S. Moghadamzadeh, R. Azmi, Y. Li, M. Kaiser, J. C. Fischer, Q. Jin, J. Maibach, I. M. Hossain, U. W. Paetzold, B. Abdollahi Nejand, *Adv. Funct. Mater.* **2021**, 32, 2107650.

[21] W. Zhang, L. Huang, W. Zheng, S. Zhou, X. Hu, J. Zhou, J. Li, J. Liang, W. Ke, G. Fang, *Nano Energy* **2022**, 96, 107078.

[22] R. He, Z. Yi, Y. Luo, J. Luo, Q. Wei, H. Lai, H. Huang, B. Zou, G. Cui, W. Wang, C. Xiao, S. Ren, C. Chen, C. Wang, G. Xing, F. Fu, D. Zhao, *Adv. Sci.* **2022**, 9, 2203210.

[23] X. Hu, J. Li, C. Wang, H. Cui, Y. Liu, S. Zhou, H. Guan, W. Ke, C. Tao, G. Fang, *Nano-Micro Lett.* **2023**, 15, 103.

[24] H. Guan, W. Zhang, J. Liang, C. Wang, X. Hu, D. Pu, L. Huang, Y. Ge, H. Cui, Y. Zou, G. Fang, W. Ke, *Adv. Funct. Mater.* **2023**, 33, 2300860.

[25] G. Su, R. Yu, Y. Dong, Z. He, Y. Zhang, R. Wang, Q. Dang, S. Sha, Q. Lv, Z. Xu, Z. Liu, M. Li, Z. a. Tan, *Adv. Energy Mater.* **2023**, 14, 2303344.

[26] W. Zhang, L. Huang, H. Guan, W. Zheng, Z. Li, H. Cui, S. Zhou, J. Liang, G. Li, T. Wang, P. Qin, W. Ke, G. Fang, *Energ. Environ. Sci.* **2023**, 5852.

[27] D. Pu, S. Zhou, H. Guan, P. Jia, G. Chen, H. Fang, S. Fu, C. Wang, H. Hushvaktov, A. Jumabaev, W. Meng, X. Wang, G. Fang, W. Ke, *Adv. Funct. Mater.* **2024**, 2314349.

[28] H. Cui, L. Huang, S. Zhou, C. Wang, X. Hu, H. Guan, S. Wang, W. Shao, D. Pu, K. Dong, J. Zhou, P. Jia, W. Wang, C. Tao, W. Ke, G. Fang, *Energ. Environ. Sci.* **2023**, 16, 5992.

[29] P. Jia, G. Chen, G. Li, J. Liang, H. Guan, C. Wang, D. Pu, Y. Ge, X. Hu, H. Cui,

S. Du, C. Liang, J. Liao, G. Xing, W. Ke, G. Fang. *Adv. Mater.* **2024**, 2400105. doi: 10.1002/adma.202400105.